PNAS RESEARCH ARTICLE | APPLIED PHYSICAL SCIENCES OPEN ACCESS

Quantum criticality enabled by intertwined degrees of freedom

Chia-Chuan Liu[a,b], Silke Paschen[c], and Qimiao Si[a,1]

Edited by J.C. Davis, University of Oxford, United Kingdom; received January 16, 2023; accepted June 20, 2023

Strange metals appear in a wide range of correlated materials. Electronic localization–delocalization and the expected loss of quasiparticles characterize beyond-Landau metallic quantum critical points and the associated strange metals. Typical settings involve local spins. Systems that contain entwined degrees of freedom offer new platforms to realize unusual forms of quantum criticality. Here, we study the fate of an SU(4) spin–orbital Kondo state in a multipolar Bose–Fermi Kondo model, which provides an effective description of a multipolar Kondo lattice, using a renormalization-group method. We show that at zero temperature, a generic trajectory in the model's parameter space contains two quantum critical points, which are associated with the destruction of Kondo entanglement in the orbital and spin channels, respectively. Our asymptotically exact results reveal an overall phase diagram, provide the theoretical basis to understand puzzling recent experiments of a multipolar heavy fermion metal, and point to a means of designing different forms of quantum criticality and strange metallicity in a variety of strongly correlated systems.

quantum criticality | strongly correlated electrons | Kondo destruction | entwined degrees of freedom | multipolar Kondo effect

Simple metals such as copper and aluminum are well described in terms of weakly correlated itinerant electrons. In a wide range of strongly correlated metals, the electrons' Coulomb repulsion is comparable to or is larger than their bandwidth (1, 2). The strong correlations are expected to cause a loss of Landau quasiparticles and the associated strange metallicity (3, 4). Correlations turn certain bare electrons into effective local degrees of freedom in the building blocks for the low-energy physics. A prototypical case is the heavy fermion metals, which feature a wide variety of quantum phases (5–7). Here, local spins are associated with the correlated $4f$-electrons. Their entanglement with the background conduction electrons gives rise to the spin-isotropic [SU(2)-symmetric] Kondo effect (8). The destruction of the Kondo effect corresponds to a localization of the $4f$-electrons, is expected to cause a loss of quasiparticles, and represents a prototype mechanism for strange metallicity and beyond-Landau quantum critical points (QCPs) (9–17).

The notion that local correlation effects drive different forms of quantum fluctuations raises the possibility of designing various types of quantum criticality by controlling local degrees of freedom. For the Kondo effect per se, various kinds of local degrees of freedom have led to a variety of Kondo states relevant to multipolar heavy fermion metals (18–25), multiorbital iron-based compounds (26–29), synthetic systems such as ultracold atoms (30) and mesoscopic devices (31–33), and other correlated settings (34–37). Recent experiments (38, 39) have motivated the idea (40, 41) that, through molecular orbitals (of limited spatial extent), Kondo effects develop as a proper description of the low-energy physics even for d-electron-based flat band systems. Meanwhile, in twisted graphene structures, there have been proposals for their understanding in terms of Kondo effects that are associated with the degrees of freedom of moiré unit cells (42–44). In these systems, different kinds of crystalline symmetries or stacking/twisting in different types of flat bands can yield various forms of local degrees of freedom. In heavy fermion metals, the nature of the local degrees of freedom is controlled by the cooperation of strong correlations, large spin–orbit coupling, and crystalline symmetry. Indeed, there is a growing list of heavy fermion metals in which the role of multipolar degrees of freedom has been explored for their quantum criticality (2, 45). These include $Pr(TM)_2Al_{20}$ (TM = Ti, V), which have nonmagnetic doublets in the ground-state manifold (46, 47), $PrOs_4Sb_{12}$, which involves field-induced local quadrupolar moments (48, 49), and $YbRu_2Ge_2$, which hosts quasi-degenerate spin and higher-rank moments (50, 51).

The hope of advancing this design principle for new types of quantum criticality is in particular triggered by recent experimental studies (52) on a heavy fermion compound $Ce_3Pd_{20}Si_6$, ref. 53 as a function of a nonthermal control parameter (magnetic field). Surprisingly, the experimental results show two stages of Kondo-destruction quantum

Significance

Melting ice illustrates how phase transitions occur by varying temperature. Quantum phase transitions appear at absolute zero temperature, when the extent to which Heisenberg's uncertainty principle affects matter is tuned through a control parameter. For a continuous transition, quantum criticality arises and influences the physics over a wide parameter range at finite temperatures. In quantum materials, the microscopic agent for quantum criticality is usually spin. Here, we show that intertwining spins, orbitals, and other degrees of freedom provide a means to design forms of quantum criticality. Our work provides the understanding of puzzling recent experiments in a spin–orbital-entwined heavy fermion metal and promises to realize unusual types of quantum criticality in a variety of strongly correlated metals.

Author affiliations: [a]Department of Physics and Astronomy, Rice Center for Quantum Materials, Rice University, Houston, TX 77005; [b]Département de Physique, Université de Montréal, Montréal, Québec H3C 3J7, Canada; and [c]Institute of Solid State Physics, Vienna University of Technology, 1040 Vienna, Austria

Author contributions: C.-C.L., S.P., and Q.S. designed research; C.-C.L., S.P., and Q.S. performed research; C.-C.L. and Q.S. analyzed data; and C.-C.L. and Q.S. wrote the paper.

The authors declare no competing interest.

This article is a PNAS Direct Submission.

[1]To whom correspondence may be addressed. Email: qmsi@rice.edu.

This article contains supporting information online at https://www.pnas.org/lookup/suppl/doi:10.1073/pnas.2300903120/-/DCSupplemental.

Published July 17, 2023.

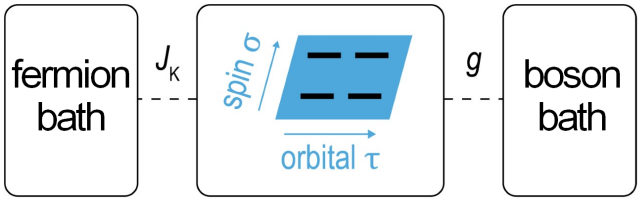

Fig. 1. Illustration of the model. The multipolar Bose–Fermi Kondo model (Eq. **1**) describes entwined local spin–orbital degrees of freedom that are coupled to a bosonic and fermionic bath.

criticality (*SI Appendix*, section A). In this system, the $4f$ electrons form a total angular momentum $J = 5/2$ state whose six-fold degeneracy is further split as dictated by the point-group symmetry (54). What lies in the ground-state manifold is the Γ_8 quartet (55), which can be represented in the pseudospin $\vec{\sigma}$ and pseudoorbital $\vec{\tau}$ bases (*SI Appendix*, section A). The competition between the Kondo entanglement in the Γ_8-manifold and the associated RKKY interactions may therefore be responsible for this sequential Kondo destruction.

The striking experimental observations motivate a well-defined theoretical question: What is the generic type of QCPs that result from this type of competition? The minimal prototype model of interest is the spin–orbital-entwined multipolar Bose–Fermi Kondo model (BFK) (52, 56), as illustrated in Fig. 1. The model involves the local degrees of freedom, containing both the spin σ and the orbital τ components, which are coupled to the fermionic and bosonic baths. The former couplings describe the (fermionic) Kondo effect, while the latter describes the collective fluctuations associated with the RKKY interactions. An outstanding question is whether a generic tuning trajectory leads to two-stage transitions or whether it could also involve a one-stage transition. The multipolar Bose–Fermi Kondo model arises as an effective Hamiltonian of the multipolar Kondo lattice model through the extended dynamical mean field theory (56–59) (*SI Appendix*, section B). In addition, we take advantage of the understanding of spin-only systems; namely, the emergence of additional fixed points beyond the Fermi liquid one in the Bose–Fermi Kondo model is insensitive to the spin symmetry (56, 60) and, furthermore, the Kondo destruction fixed points of the Bose–Fermi model are realized in the corresponding Kondo lattice model through the extended dynamical mean field analysis. Accordingly, we i) will analyze the multipolar Bose–Fermi Kondo model in its Ising-anisotropic case to allow for comprehensive analytical studies, though we expect that the conclusion that additional fixed points develop in this model will apply to the spin-isotropic case as well and ii) expect that the additional fixed points that we identify in the multipolar Bose–Fermi Kondo model will be realized as Kondo destruction quantum critical points in the multipolar Kondo lattice model.

We thus study the multipolar Bose–Fermi Kondo model at zero temperature. By using a Coulomb-gas representation of the Bose–Fermi Kondo model, we carry out analytical renormalization-group (RG) calculations that are controlled by an expansion in terms of a small quantity ϵ (defined in Eq. **3**). We uncover an overall phase diagram at zero temperature, which reveals the mechanism for the sequential Kondo destruction and shows that it appears for any generic trajectory in the phase diagram. Our asymptotically exact theory points to a design principle for beyond-Landau quantum criticality and strange metallicity in a variety of other strongly correlated systems, including d-electron-based flat band systems and moiré structures.

Results

Sequential Destruction of Multipolar Kondo Entanglement. Our key findings are visualized in terms of an overall phase diagram presented in the $g_{\sigma z}$-$g_{\tau z}$ parameter space, as illustrated in Fig. 2. Here, $g_{\sigma z}$ and $g_{\tau z}$ are the couplings of the local multipolar moment to the bosonic fields in the spin and orbital channels, respectively. The fermionic Kondo couplings are kept fixed. Our main results are as follows:

- In the special case with the spin and orbital bosonic couplings being equal, $g_{\sigma z} = g_{\tau z}$, we identify a critical fixed point that is accessible by the ϵ-expansion. This critical point, marked by the red point in Fig. 2, describes a one-stage transition for the destruction of the SU(4) spin–orbital Kondo effect.
- We find that the anisotropy between these two bosonic couplings is relevant in the RG sense. This implies that the one-stage Kondo destruction cannot describe the quantum phase transition along a generic trajectory in the phase diagram.
- Moreover, we are able to determine the complete phase diagram asymptotically exactly, as shown in Fig. 2. This is made possible by realizing that all the phase boundaries meet at the equal-bosonic-coupling critical fixed point, near which the run-away RG flows are still small within the ϵ-expansion. It is further substantiated by a more comprehensive RG analysis presented in *SI Appendix*, sections C and D.

The overall phase diagram implies two stages of Kondo-destruction QCPs for any generic tuning trajectory at zero temperature, one each in the spin and orbital channels despite their entwining in the Hamiltonian. This is illustrated by the sequence of quantum phase transitions along the solid black lines in Fig. 2.

Model and Solution Methods. We now specify the model and describe the setup for our asymptotically exact analysis. The

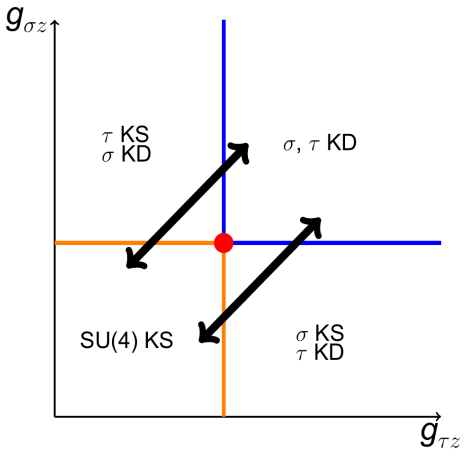

Fig. 2. The overall phase diagram. Presented here is the phase diagram in the $g_{\sigma z}$-$g_{\tau z}$ parameter space, for fixed Kondo couplings, of the model given in Eq. **1**. KD and KS refer to the phases with Kondo destruction and Kondo screening, respectively, whereas σ and τ refer to spin and orbital (c.f., Fig. 1), respectively. The black arrows mark generic trajectories in the parameter space that correspond to the tuning of a nonthermal physical control parameter. The overall phase diagram implies two stages of Kondo destruction along any generic tuning trajectory.

multipolar Bose–Fermi Kondo model, schematically described by Fig. 1, is given by the following Hamiltonian:

$$H_{\rm BFK} = H_0 + H_{\rm K,0} + H_{\rm BK}. \quad [1]$$

Here, H_0 is the noninteracting part for the conduction electron $c_{p,i\alpha}$ and the bosonic baths $\vec{\phi}\kappa, q$ (where $\kappa = \sigma, \tau, m$):

$$H_0 = \sum_{p,i\alpha} \epsilon_p c^\dagger_{p,i\alpha} c_{p,i\alpha} + \sum_q W_q \left(\vec{\phi}^\dagger_{\sigma,q} \cdot \vec{\phi}_{\sigma,q} + \vec{\phi}^\dagger_{\tau,q} \cdot \vec{\phi}_{\tau,q} + \vec{\phi}^\dagger_{m,q} \cdot \vec{\phi}_{m,q} \right). \quad [2]$$

To set up controlled RG calculation, we introduce an expansion parameter ϵ, which is defined through the bosonic spectrum W_q:

$$\sum_q \left[\delta(\omega - W_q) - \delta(\omega + W_q) \right] = \left(\frac{K_0^2}{\pi} \right) |\omega|^{1-\epsilon} \operatorname{sgn} \omega, \quad [3]$$

with $0 < \epsilon < 1$, and for $|\omega| < \Lambda$, which specifies a high-energy cutoff scale. The fermionic Kondo coupling between the local multipolar moment and conduction electrons is as follows:

$$H_{\rm K,0} = \left[J_\sigma \vec{\sigma} \cdot \vec{\sigma}_c + J_\tau \vec{\tau} \cdot \vec{\tau}_c + 4 J_M (\vec{\sigma}_i \otimes \vec{\tau}) \cdot (\vec{\sigma}_c \otimes \vec{\tau}_c) \right], \quad [4]$$

where $\vec{\sigma}(\vec{\tau})$ and $\vec{\sigma}_c(\vec{\tau}_c)$ are the spin (orbital) operators of the single impurity and the conduction electrons, respectively. Further details and definitions are given in *Methods*, Section I.

Finally, the coupling between the local multipolar moment and the bosonic bath is given by:

$$H_{\rm BK} = g_{\sigma z} \sigma_z \phi_{\sigma z} + g_{\tau z} \tau_z \phi_{\tau z} + g_m (\sigma_z \otimes \tau_z) \phi_m, \quad [5]$$

where $\vec{\phi}_\kappa = \sum_q \left(\vec{\phi}_{\kappa,q} + \vec{\phi}^\dagger_{\kappa,-q} \right)$ with $\kappa = \sigma, \tau, m$. We focus on the Ising-anisotropic case for the couplings in both the spin and orbital channels ($g_{\sigma z}$ and $g_{\tau z}$, respectively) as well as for the spin–orbital mixed coupling (g_m). The BFK model H_{BFK} (Eq. **1**) is mapped from a multipolar Kondo lattice model that contains a lattice of local levels with a four-fold degeneracy by the scheme of extended dynamical mean field theory (56–59).

We now summarize how to set up the framework to tackle this rich problem using the (asymptotically exact) RG approach. We aim to determine the generic phase diagram in the $g_{\sigma z}$-$g_{\tau z}$ parameter space. In other words, we fix the fermionic Kondo couplings and vary $g_{\sigma z}$ and $g_{\tau z}$, and we can keep the mixed bosonic coupling $g_m = 0$ (*Methods*, Section I). We are able to set up systematic RG calculations using a Coulomb-gas representation, as described in some detail in (*Methods*, Section I). We achieve this by dividing the analysis into two steps. First, we analyze the problem along a fine-tuned trajectory in the phase diagram: along the diagonal in the $g_{\sigma z}$-$g_{\tau z}$ space, viz. the trajectory "I" in Fig. 3*A*. This analysis leads to an anchoring point, which allows us to determine the sequence of quantum phase transitions along generic trajectories of the phase diagram.

Quantum Phase Transitions: Fine-Tuned Case. We now carry out RG calculation of the spin–orbital coupled Bose–Fermi Kondo model (Eq. **1**). As outlined in *Methods*, Section I, we will start from trajectory "I" of Fig. 3*A*, which corresponds to the fine-tuned case of equal bosonic couplings in the spin and orbital channels, $g_{\sigma z} = g_{\tau z}$. We demonstrate a critical point

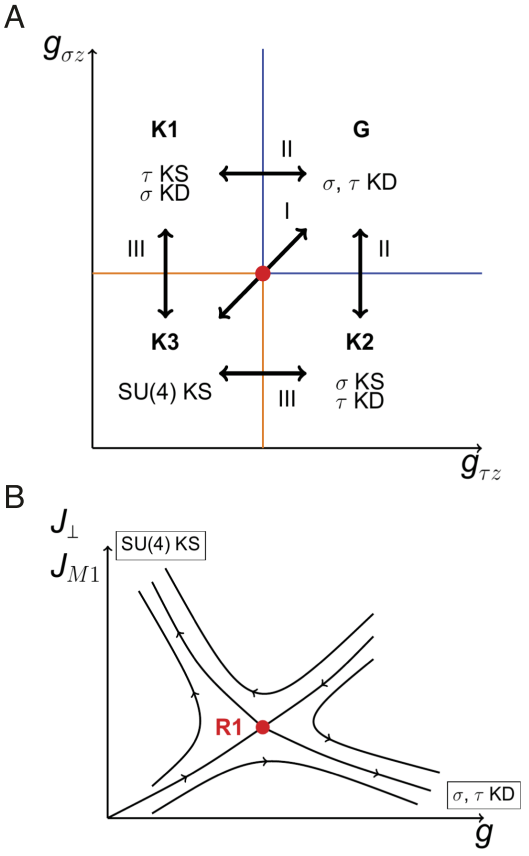

Fig. 3. Renormalization-group analysis. (*A*) Trajectories in the parameter space of the BFK model (Eq. **1**), marked as "I"–"III," along which the RG analyses are carried out in steps. The labels "G," "K1," "K2," and "K3" describe the RG fixed points for the corresponding phases. (*B*) RG flow diagram of the reduced beta functions (Eq. **7**), where $g = g_{\sigma z} = g_{\tau z}$. "**R1**" marks the unstable fixed point that captures the transition along the fine-tuned trajectory "I" of (*A*).

[marked by the red solid point in Fig. 3*A*] that is accessible by an ϵ-expansion in our RG analysis. It describes a direct transition from the spin and orbital Kondo-destroyed (KD) phase to the fully (spin or orbital) Kondo-screened (KS) phase. It will be shown in the next section that, by analyzing the vicinity of this critical point, we can determine the structure of the overall phase diagram.

Generally, the total number of coupling constants is seven (*Methods*, Section I). However, under the trajectory $g_{\sigma z} = g_{\tau z} = g$, some of the coupling constants are irrelevant or can be combined due to the symmetry constraint, and thus, the numbers of relevant RG equations (the beta functions) are substantially reduced. We leave the details in *SI Appendix*, section D and present the final reduced beta functions and their analysis in (*Methods*, Section II). The RG beta functions are expressed in terms of $y \propto J_{\sigma\perp} = J_{\tau\perp}$, which flips either spin or orbital indices, $M \propto g^2_{\sigma z} = g^2_{\tau z} = g^2$, and $y_1 \propto J_{M1}$, which is the part of the Kondo coupling J_M that flips both the spin and orbital indices (*SI Appendix*, Eq. **S.8** in section C).

From these reduced beta functions, Eq. **7**, we identify a critical point marked by the red dot in Fig. 3 and labeled as **R1**. Importantly, this fixed point is accessible by our ϵ-expansion. It has one relevant direction and separates the spin and orbital KD phase from the SU(4) KS phase, which we call **K3** for latter convenience. Because **R1** is accessible by the ϵ-expansion, we can address what happens in the vicinity of this fixed point. We will show in the next section that any small asymmetry

between $g_{\tau z}$ and $g_{\sigma z}$ around **R1** is relevant in the RG sense. As a result, the direct phase transition between spin and orbital KD phase and SU(4) KS phase is fine-tuned. In other words, this direct transition occurs at a point in the parameter space—the red dot in Fig. 3 *A* and *B*—instead of through a boundary line.

Quantum Phase Transitions: Generic Cases. So far we have considered the case of equal bosonic couplings in the spin and orbital channels, i.e., $g_{\sigma z} = g_{\tau z} = g$. However, these two couplings are generically different. Thus, we have to determine the quantum phase transitions along trajectories away from the diagonal in the $g_{\sigma z}$-$g_{\tau z}$ parameter space. We find that there are two sets of trajectories, which are marked by "II" and "III" in Fig. 3*A*. We describe our analyses of these two cases in turn.

We next consider the transition between the spin and orbital KD phase and the spin or orbital KS phase. Importantly, we do so by starting from the RG trajectory around the critical point **R1** where $g_{\sigma z} = g_{\tau z} = g^*$ between the spin and orbital KD and the SU(4) KS phases. As we have just alluded to, around **R1**, any small asymmetry between $g_{\tau z}$ and $g_{\sigma z}$ is relevant with the scaling dimension $\sqrt{2\epsilon}$ (up to the order $\sqrt{\epsilon}$) in RG sense.

Consider first the case with a slight increase of the coupling constant $g_{\tau z}$, while keeping all the other parameters fixed; in other words, now $g_{\tau z} > g_{\sigma z} = g^*$. The RG trajectory will flow toward $g_{\tau z} \to \infty$. We can then vary $g_{\sigma z}$ to map out the RG flow. The corresponding trajectory in the phase diagram is denoted as an arrow (II) in Fig. 3*A*. Along this trajectory, the reduced beta functions are determined (see *Methods*, Eq. **8**) in terms of $y_2 \propto J_{\sigma\perp}$, which flips only the orbital indices, and $M^\sigma \propto g_{\sigma z}^2$.

From the reduced beta functions (Eq. **8**), one can identify another critical fixed point $(y_2^*, M^{\sigma *}) = \left(\frac{\sqrt{\epsilon}}{2}, 1\right)$. This fixed point has one relevant direction with scaling dimension $\sqrt{2\epsilon}$ (up to the order $\sqrt{\epsilon}$) and separates the spin KS phase $(y_2 \to \infty, M^\sigma \to 0)$ from the spin and orbital KD phase $(y_2 \to 0, M^\sigma \to \infty)$.

The schematic RG flow structure is shown in Fig. 4, where the spin and orbital KD phase and the spin KS phase, denoted as **G** and **K1**, respectively, are separated by the critical point denoted as **F1**. Based on this RG structure, we establish the transition between the spin and orbital KD phase and the spin KS phase. By applying a precisely parallel analysis, we establish the phase transition between spin and orbital KD phase and the orbital KS phase; we name the associated critical point as **F2**.

We have so far analyzed the transitions out of the spin and orbital KD phase. This phase can transit into the spin or orbital KS phase without fine-tuning the parameters. It can also transit into the SU(4) KS phase by fine-tuning the parameters.

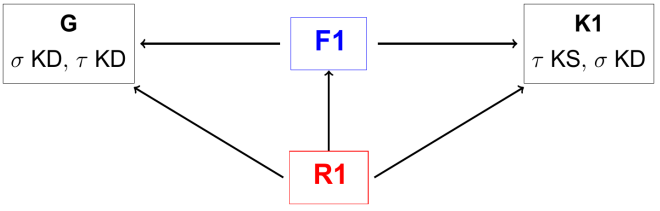

Fig. 4. The schematic renormalization-group flow structure. Illustrated here is the RG flow structure of the phase transition between the orbital and spin KD phase and the spin KS phase denoted as **G** and **K1**, respectively. Around the multicritical point **R1**, once the $g_{\sigma z}$ is slightly enlarged, the RG trajectory will flow toward **F1**, which is the generic critical point separating **G** and **K1**.

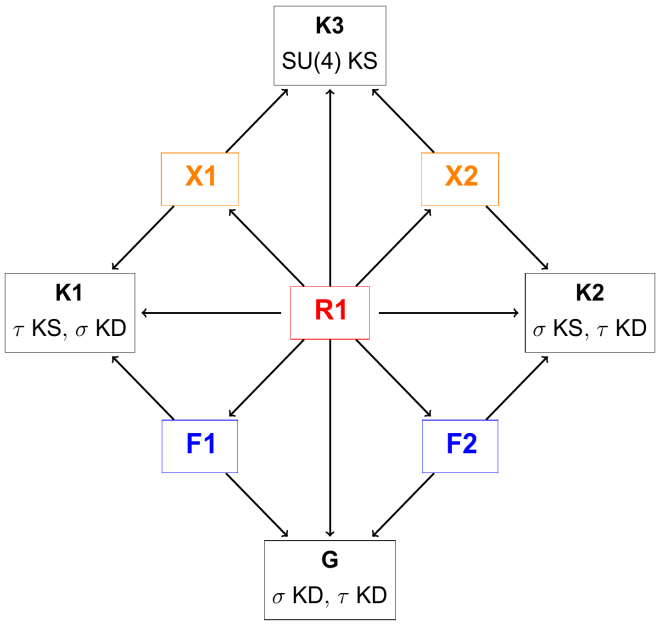

Fig. 5. The schematic structure of the fixed points. Illustrated here are the structure of the fixed points and the relative RG flow of the BFK model (Eq. **1**), as derived from the RG analysis. KS and KD denote the Kondo-screened and Kondo-destroyed fixed points, respectively. The boxes **K1**–**K3** are different kinds of strong Kondo coupling fixed points, and the box **G** is the spin and orbital KD fixed point. The red box **R1** is a multicritical point between spin and orbital KD phase and SU(4) KS phase. The blue-boxed **F1**–**F2** are the generic critical point separating different types the spin and orbital KD phases to either spin or orbital KS phases. Because the strong Kondo coupling fixed points **K1**, **K2**, and **K3** are stable fixed points, they are separated by the generic critical points, denoted as orange boxes **X1** and **X2**.

Because the spin or orbital KS phase and the SU(4) KS phase correspond to different stable strong coupling fixed points, there must be other generic critical points that separate them. These generic critical points describe the phase transition between the spin or orbital KS phase and the SU(4) KS phase, as shown in the phase diagram trajectory denoted as the dashed arrow (III) in Fig. 3*A*. Here, we would like to finally establish the transition between the spin or orbital KS phase and the SU(4) KS phase, which corresponds to the trajectories (III) in Fig. 3*A*.

Again, we focus on the RG trajectory around the critical point **R1** where $g_{\sigma z} = g_{\tau z} = g^*$ between the spin and orbital KD and SU(4) KS phases. If we keep all the other parameters fixed but just slightly decrease the coupling constant $g_{\sigma z}$, that is, $g_{\sigma z} < g_{\tau z} = g^*$, then the RG trajectory will flow toward $g_{\sigma z} \to 0$. We can then vary $g_{\tau z}$ to explore the RG trajectory. The corresponding trajectories in the phase diagram are denoted as the arrow III in Fig. 3*A*.

However, unlike **R1** and **F1**, the real locations of the **X1** are harder to identify directly from the beta functions. To proceed, we exploit the property of the critical point **R1** that we alluded to earlier: Here, all of the fugacity y is $\sim \sqrt{\epsilon}$ around **R1**. Near **R1**, one can thus neglect in a controlled way the higher-order terms of $\sqrt{\epsilon}$ in the beta functions of the fugacity (see *SI Appendix*, section D for more details), and in the end, the reduced beta functions are determined (see *Methods*, Eq. **9**) in terms of y_1, M^τ, and $y_3 \propto J_{\tau\perp}$.

From the reduced beta functions (Eq. **9**), we identify a critical line $\left(y_1^*, y_3^*, M^{\tau *}\right) = \left(a, \frac{\sqrt{\epsilon - 4a^2}}{2}, 1\right)$ where a is a constant, which separates the spin and orbital KS phase from the spin KS phase and corresponds to the critical point **X1** in Fig. 5 with scaling

dimension $\sqrt{2\epsilon}$. By a parallel analysis, the transition between the spin and orbital KS phase and the orbital KS phase can also be established.

Phase Diagram and the Sequential Kondo Destruction. Based on the above, we have established the overall phase diagram, which is shown in Fig. 2. This phase diagram is also seen through a complete RG flow, Fig. 3*A*, which combines the RG flows along the various trajectories we have described in the previous sections (A complementary, and more comprehensive, way of deriving this complete RG flow is given in *SI Appendix*, section D). We summarize the characterization of the various phases and their transitions as follows:

- The boxes **K1**–**K3** are different kinds of strong Kondo coupling fixed points, and the box **G** is the spin and orbital KD fixed point. These fixed points are all stable according to the beta functions (*SI Appendix*, Eq. **S.44**) in *SI Appendix*, section C, and thus describe phases of matter.
- The red box **R1** is a multicritical point between the spin and orbital KD phase and SU(4) KS phase since there are two relevant directions around it.
- The blue-boxed **F1**–**F2** are the generic critical point separating different types the spin and orbital KD phases to either spin or orbital KS phases.
- Because the strong Kondo coupling fixed points **K1**, **K2**, and **K1** are stable fixed points, they are separated by the generic critical points **X1** and **X2**. The generic critical points **X1** and **X2** control the critical phenomena of the trajectories III in Fig. 3*A*.

The solid black arrows in Fig. 2 marks the generic tuning trajectories in the zero-temperature phase diagram. Along each of such trajectories, two stages of Kondo destruction take place, each characterizing a QCP in the spin or orbital channel. This asymptotically exact result provides a firm theoretical basis to understand the field-induced quantum phase transitions that have been experimentally observed in $Ce_3Pd_{20}Si_6$ (52).

Discussion

In this work, we have performed a detailed renormalization-group analysis of a spin–orbital-entwined Bose–Fermi-Kondo model, which is mapped from a multipolar Kondo lattice model. We are able to determine the overall phase diagram at zero temperature, which reveals the mechanism for the sequential Kondo destruction and shows that it appears for any generic trajectory in the phase diagram. As such, our results provide a firm theoretical basis for understanding the surprising experimental results in the heavy fermion metal $Ce_3Pd_{20}Si_6$ (52). More generally, our work elucidates the quantum criticality in spin–orbital-coupled heavy fermion systems.

Our asymptotically exact theoretical results also make it clear how the entwining of spins, orbitals, and other quantum numbers in local degrees of freedom allows for unexpected types of quantum criticality and associated strange metallicity. This represents a design principle for creating and realizing new forms of quantum criticality and associated strange metallicity: The cooperation of strong correlations, large spin–orbit coupling, and crystalline symmetry represents a robust means to create varied local degrees of freedom; and the tuning of such strongly correlated systems can realize a sequence of beyond-Landau quantum critical points. Beyond heavy fermion metals, effective local degrees of freedom have also been advanced for pertinent molecular orbitals of *d*-electron-based flat band systems (38–41) and for moiré states of twisted structures (42–44). Thus, we expect this design procedure to operate not only in multipolar heavy fermion metals but also in transition-metal compounds, synthetic systems such as moiré structures, and beyond.

Methods

I. Model and the Renormalization-Group Method. In the definition of the model, Eqs. **1**–**4**, the spin and orbital operators of the conduction electrons are defined as:

$$\vec{\sigma}_c = \frac{1}{2}\sum_{i,\alpha\beta} c^\dagger_{i\alpha}\vec{s}_{\alpha\beta}c_{i\beta},$$
$$\vec{\tau}_c = \frac{1}{2}\sum_{ij,\alpha} c^\dagger_{i\alpha}\vec{t}_{ij}c_{j\alpha}, \qquad [6]$$
$$\vec{\sigma}\otimes\vec{\tau}_c = \frac{1}{4}\sum_{ij,\alpha\beta} c^\dagger_{i\alpha}\vec{s}_{\alpha\beta}\otimes\vec{t}_{ij}c_{j\beta}.$$

Here, we use α, β, and i, j to denote the spin and orbital indices, respectively. Thus, $\vec{s}_{\alpha\beta}$ and $\vec{t}_{ij}$ are Pauli matrices in the spin and orbital subspaces, respectively. For the fermionic Kondo Hamiltonian alone, the anisotropy in the couplings is generically unimportant as the system restores the SU(4) symmetry in the Kondo-entangled ground state (8). We have therefore chosen the bare Kondo Hamiltonian to be SU(2) symmetric in the spin as well as in the orbital sector, with an overall SU(2)⊗SU(2) symmetry. The full renormalized Kondo Hamiltonian (*SI Appendix*, Eq. **S.8**) for the later RG analysis is shown in *SI Appendix*, section C.

We now describe the framework to tackle this rich problem using the (asymptotically exact) RG approach. Further details can be found in *SI Appendix*, section C.

First, our goal is to study the generic phase diagram in the $g_{\sigma z}$-$g_{\tau z}$ parameter space. In other words, we fix the fermionic Kondo couplings and vary $g_{\sigma z}$ and $g_{\tau z}$. For this purpose, it suffices to keep the mixed bosonic coupling $g_m = 0$. A nonvanishing but small g_m does not modify the structure of the phase diagram, as we show in *SI Appendix*, section E. To proceed, we use a bosonization approach to represent the BFK model (Eq. **1**) in terms of a Coulomb gas, from which a controlled RG calculation based on an expansion in ϵ is possible (60–62).

We note that the Coulomb-gas RG calculation is based on a dilute-instanton expansion, which is nonperturbative in stiffness constants but perturbative in terms of fugacities (60).

Second, the Ising couplings of H_{BK} (Eq. **5**) break not only the SU(4) symmetry but also the smaller SU(2) × SU(2) symmetry. While the Kondo couplings in H_K respect the SU(2) × SU(2) symmetry, under the RG flow, these couplings will generically become spin anisotropic. It turns out that one needs to consider five types of Kondo couplings. Together with the spin and orbital Ising couplings $g_{\sigma z}$ and $g_{\tau z}$ of H_{BK} (Eq. **5**), the total number of RG coupling constants is seven. The large number of the RG charges makes it a challenge to determine the overall RG flow structure. We are able to accomplish this goal by analyzing the problem in several steps.

Crucially, we take the first step to be a fine-tuned trajectory in the phase diagram. Recall that the $g_{\sigma z}$-$g_{\tau z}$ parameter space is of our interest. For clarity, we visualize this parameter space in Fig. 3*A*, which marks the relevant phases. The fine-tuned trajectory we focus our initial analysis on corresponds to identical couplings to the bosonic baths in the spin and orbital sectors. It goes along the diagonal in the $g_{\sigma z}$-$g_{\tau z}$ space and is marked as trajectory "I." The result of the analysis of this fine-tuned trajectory provides a anchoring point, which allows us to determine the sequence of quantum phase transitions along generic trajectories of the phase diagram.

We note that it is possible to rigorously establish the phase diagram, Fig. 3*A*, through a comprehensive RG analysis without taking the fine-tuned trajectory "I" as the starting anchoring point. This is described in *SI Appendix*, sections C and D).

We choose to present the step-by-step analysis here in the main text, given that it reveals the underlying physics in a considerably more transparent way.

II. RG Equations and Analysis: Fine-Tuned Case. The RG analysis, described in *SI Appendix*, section D, leads to the following reduced beta functions:

$$\begin{aligned}\frac{dy_1}{dl} &= (1-2M)\,y_1 + 2y^2,\\ \frac{dy}{dl} &= (1-M)\,y + 2y_1 y,\\ \frac{dM}{dl} &= \left(\epsilon - 4y_1^2 - 4y^2\right) M.\end{aligned} \quad [7]$$

Note that we can set $J_{\sigma\perp} = J_{\tau\perp}$, given that we are considering a path in the parameter space that preserves the symmetry $\sigma \leftrightarrow \tau$. From these reduced beta functions (Eq. **7**), we identify a critical point (up to the order $\sqrt{\epsilon}$) at $\left(y_1^*, y^*, M^*\right) = \left(\frac{-1+\sqrt{1+12\epsilon}}{12}, \frac{\sqrt{-1+12\epsilon+\sqrt{1+12\epsilon}}}{6\sqrt{2}}, \frac{5+\sqrt{1+12\epsilon}}{6}\right) \cong \left(0, \frac{\sqrt{\epsilon}}{2}, 1\right)$. This fixed point has one relevant direction with the scaling dimension $\sqrt{2\epsilon}$ and separates the spin and orbital KD phase $(y_1 \to 0, y \to 0, M \to \infty)$ from the SU(4) KS phase $(y_1 \to \infty, y \to \infty, M \to 0)$(64). The RG flow structure of the reduced beta functions (Eq. **7**) is plotted in Fig. 3. For latter convenience, we name SU(4) KS phase as **K3** and the critical point (the red dot in Fig. 3) as **R1**.

For our analysis, one feature of the fixed point **R1** plays a crucial role. While the fixed-point value for the RG charge M is O(1), the values for the RG charges (the fugacities) y_1 and y are of order $\sqrt{\epsilon}$. Because of this feature, the quardratic-in-y_α terms in the beta functions of the fugacities turn out to be unimportant for both RG flow structure and the leading order of the scaling dimensions. The same conclusion is also seen in the scaling dimensions of the RG variables near **R1**; to the leading nonvanishing order in ϵ, they are the same regardless of whether the quardratic-in-y_α terms are kept in the beta-functions of the fugacities. In the next section, we will see how this allows us to determine the overall structure of the phase diagram by expanding the RG equations around the fixed point **R1**. In particular, it allows us to carry out a complete analysis of the quantum phase transition along trajectory "III," which otherwise would have been much harder to achieve.

III. RG Equations for the Generic Case—Trajectory II. Along this trajectory, the reduced beta functions are calculated to be as follows:

$$\begin{aligned}\frac{dy_2}{dl} &= (1-M^\sigma)\,y_2,\\ \frac{dM^\sigma}{dl} &= \left(\epsilon - 4y_2^2\right) M^\sigma.\end{aligned} \quad [8]$$

Again, we leave the details of the derivation to *SI Appendix*, section D.

IV. RG Equations for the Generic Case—Trajectory III. Along this trajectory, the reduced beta functions are as follows:

$$\begin{aligned}\frac{dy_1}{dl} &= (1-M^\tau)\,y_1,\\ \frac{dy_3}{dl} &= (1-M^\tau)\,y_3,\\ \frac{dM^\tau}{dl} &= \left(\epsilon - 4y_1^2 - 4y_3^2\right) M^\tau.\end{aligned} \quad [9]$$

Data, Materials, and Software Availability. All data needed to evaluate the conclusions in the paper are presented in the paper and/or *SI Appendix*.

Note Added in Proof. The sequential Kondo destruction that we identify in the minimal prototype multipolar model has now also been seen in a related model that contains additional couplings and has continuous spin symmetry (S. E. Han, D. J. Schultz, and Y. B. Kim, "Microscopic theory of multistage Fermi surface reconstruction in higher-rank moment quantum materials").

ACKNOWLEDGMENTS. We thank Ang Cai, Kevin Ingersent, Emilian Nica, and Rong Yu for useful discussions. The work has been supported in part by the NSF Grant No. DMR-2220603 and the Robert A. Welch Foundation Grant No. C-1411. Work in Vienna has been supported by the Austrian Science Fund SFB F86 and I5868 and the European Community (H2020 Project No. 824109). One of us (Q.S.) acknowledges the hospitality of the Aspen Center for Physics, which is supported by the NSF Grant No. PHY-1607611.

1. B. Keimer, J. E. Moore, The physics of quantum materials. *Nat. Phys.* **13**, 1045 (2017).
2. S. Paschen, Q. Si, Quantum phases driven by strong correlations. *Nat. Rev. Phys.* **3**, 9–26 (2021).
3. H. Hu, L. Chen, Q. Si, Quantum critical metals: Dynamical Planckian scaling and loss of quasiparticles. arXiv [Preprint] (2022). http://arxiv.org/abs/2210.14183 (Accessed 6 July 2023).
4. P. W. Phillips, N. E. Hussey, P. Abbamonte, Stranger than metals. *Science* **377**, eabh4273 (2022).
5. G. R. Stewart, Non-Fermi-liquid behavior in d- and f-electron metals. *Rev. Mod. Phys.* **73**, 797–855 (2001).
6. P. Coleman, A. J. Schofield, Quantum criticality. *Nature* **433**, 226–229 (2005).
7. S. Kirchner *et al.*, Colloquium: Heavy-electron quantum criticality and single-particle spectroscopy. *Rev. Mod. Phys.* **92**, 011002 (2020).
8. A. C. Hewson, *The Kondo Problem to Heavy Fermions* (Cambridge University Press, 1993).
9. Q. Si, S. Rabello, K. Ingersent, J. Smith, Locally critical quantum phase transitions in strongly correlated metals. *Nature* **413**, 804–808 (2001).
10. P. Coleman, C. Pépin, C. Q. Si, R. Ramazashvili, How do Fermi liquids get heavy and die? *J. Phys. Condens. Matter* **13**, R723–R738 (2001).
11. T. Senthil, M. Vojta, S. Sachdev, Weak magnetism and non-Fermi liquids near heavy-fermion critical points. *Phys. Rev. B* **69**, 035111 (2004).
12. A. Schröder *et al.*, Onset antiferromagnetism in heavy-fermion metals. *Nature* **407**, 351 (2000).
13. S. Paschen *et al.*, Hall-effect evolution across a heavy-fermion quantum critical point. *Nature* **432**, 881 (2004).
14. H. Shishido, R. Settai, H. Harima, Y. Onuki, A drastic change of the Fermi surface at a critical pressure in $CeRhIn_5$: dHvA study under pressure. *J. Phys. Soc. Jpn.* **74**, 1103 (2005).
15. T. Park *et al.*, Isotropic quantum scattering and unconventional superconductivity. *Nature* **456**, 366 (2008).
16. L. Prochaska *et al.*, Singular charge fluctuations at a magnetic quantum critical point. *Science* **367**, 285 (2020).
17. D. H. Nguyen *et al.*, Superconductivity in an extreme strange metal. *Nat. Commun.* **12**, 4341 (2021).
18. A. Patri, I. Khait, Y. B. Kim, Emergent non-Fermi-liquid phenomena in multipolar quantum impurity systems. *Phys. Rev. Res.* **2**, 013257 (2020).
19. A. Patri, Y. B. Kim, Critical theory of non-fermi liquid fixed point in multipolar Kondo problem. *Phys. Rev. X* **10**, 041021 (2020).
20. H.-H. Lai *et al.*, Kondo destruction and multipolar order–Implications for heavy Fermion quantum criticality. arXiv [Preprint] (2018). http://arxiv.org/abs/1807.09258 (Accessed 6 July 2023).
21. J. S. Van Dyke, G. H. Zhang, R. Flint, Field-induced ferrohastatic phase in cubic non-Kramers doublet systems. *Phys. Rev. B* **100**, 205122 (2019).
22. G. H. Zhang, J. S. Van Dyke, R. Flint, Cubic hastatic order in the two-channel Kondo-Heisenberg model. *Phys. Rev. B* **98**, 235143 (2018).
23. C. J. Bolech, N. Andrei, Solution of the multichannel Anderson impurity model: Ground state and thermodynamics. *Phys. Rev. B* **71**, 205104 (2005).
24. C. J. Bolech, N. Andrei, Solution of the two-channel Anderson impurity model: Implications for the heavy fermion UBe_{13}. *Phys. Rev. Lett.* **88**, 237206 (2002).
25. D. L. Cox, A. Zawadowski, Exotic Kondo effects in metals: Magnetic ions in a crystalline electric field and tunnelling centres. *Adv. Phys.* **47**, 599 (1998).
26. Q. Si, R. Yu, E. Abrahams, High-temperature superconductivity in iron pnictides and chalcogenides. *Nat. Rev. Mater.* **1**, 16017 (2016).
27. C. Aron, G. Kotliar, Analytic theory of Hund's metals: A renormalization group perspective. *Phys. Rev. B* **91**, 041110 (2015).
28. E. Walter *et al.*, Uncovering non-fermi-liquid behavior in hund metals: Conformal field theory analysis of an $SU(2)\times SU(3)$ spin-orbital Kondo model. *Phys. Rev. X* **10**, 031052 (2020).
29. T. T. Ong, P. Coleman, Local quantum criticality of an iron-pnictide tetrahedron. *Phys. Rev. Lett.* **108**, 107201 (2012).
30. Y. Nishida, SU(3) orbital Kondo effect with ultracold atoms. *Phys. Rev. Lett.* **111**, 135301 (2013).
31. K. Le Hur, P. Simon, Smearing of charge fluctuations in a grain by spin-flip assisted tunneling. *Phys. Rev. B* **67**, 201308 (2003).
32. R. M. Potok, I. G. Rau, H. Shtrikman, Y. Oreg, D. Goldhaber-Gordon, Observation of the two-channel Kondo effect. *Nature* **446**, 167–171 (2007).
33. A. Mitchell, A. Liberman, E. Sela, I. Affleck, SO(5) non-Fermi liquid in a Coulomb box device. *Phys. Rev. Lett.* **126**, 147702 (2021).
34. A. Horvat, R. Zitko, J. Mravlje, Low-energy physics of three-orbital impurity model with Kanamori interaction. *Phys. Rev. B* **94**, 165140 (2016).
35. J. G. Rau, H.-Y. Kee, Symmetry breaking via hybridization with conduction electrons in frustrated Kondo lattices. *Phys. Rev. B* **89**, 075128 (2014).

36. P. Coleman, L. B. Ioffe, A. M. Tsvelik, Simple formulation of the two-channel Kondo model. *Phys. Rev. B* **52**, 6611 (1995).
37. I. Affleck, A. W. W. Ludwig, Critical theory of overscreened Kondo fixed points. *Nucl. Phys. B* **360**, 641 (1991).
38. L. Ye *et al*., A flat band-induced correlated kagome metal. arXiv [Preprint] (2021). http://arxiv.org/abs/2106.10824 (Accessed 6 July 2023).
39. S. A. Ekahana *et al*., Anomalous quasiparticles in the zone center electron pocket of the kagomé ferromagnet Fe_3Sn_2. arXiv [Preprint] (2022). http://arxiv.org/abs/2206.13750 (Accessed 6 July 2023).
40. H. Hu and Q. Si, *Coupled topological flat and wide bands: Quasiparticle formation and destruction*. arXiv [Preprint] (2022). http://arxiv.org/abs/2209.10396 (Accessed 6 July 2023).
41. L. Chen *et al*., Emergent flat band and topological Kondo semimetal driven by orbital-selective correlations. arXiv [Preprint] (2022). http://arxiv.org/abs/2212.08017 (Accessed 6 July 2023).
42. A. Ramires, J. L. Lado, Emulating heavy fermions in twisted trilayer graphene. *Phys. Rev. Lett.* **127**, 026401 (2021).
43. Z.-D. Song, B. A. Bernevig, Magic-angle twisted bilayer graphene as a topological heavy fermion problem. *Phys. Rev. Lett.* **129**, 047601 (2022).
44. D. Guerci *et al*., Chiral Kondo lattice in doped $MoTe_2/WSe_2$ bilayers. *Sci. Adv.* **9**, eade7701 (2023).
45. S. Paschen, J. J. Larrea, Ordered phases and quantum criticality in cubic heavy fermion compounds. *J. Phys. Soc. Jpn* **83**, 061004 (2014).
46. A. Sakai, S. Nakatsuji, Kondo effects and multipolar order in the cubic $PrTr_2Al_{20}$ (Tr=Ti, V). *J. Phys. Soc. Jpn.* **80**, 063701 (2011).
47. Y. Shimura *et al*., Field-induced quadrupolar quantum criticality in PrV_2Al_{20}. *Phys. Rev. B* **91**, 241102(R) (2015).
48. A. McCollam, B. Andraka, S. R. Julian, Fermi volume as a probe of hidden order. *Phys. Rev. B* **88**, 075102 (2013).
49. E. D. Bauer, N. A. Frederick, P. C. Ho, V. S. Zapf, M. B. Maple, Superconductivity and heavy fermion behavior in $PrOs_4Sb_{12}$. *Phys. Rev. B* **65**, 100506 (2002).
50. E. W. Rosenberg, J.-H. Chu, J. P. C. Ruff, A. T. Hristov, I. R. Fisher, Divergence of the quadrupole-strain susceptibility of the electronic nematic system $YbRu_2Ge_2$. *Proc. Natl. Acad. Sci. U.S.A.* **116**, 7232–7237 (2019).
51. H. S. Jeevan, C. Geibel, Z. Hossain, Quasiquartet crystal-electric-field ground state with possible quadrupolar ordering in the tetragonal compound $YbRu_2Ge_2$. *Phys. Rev. B* **73**, 020407 (2006).
52. V. Martelli *et al*., Sequential localization of a complex electron fluid. *Proc. Natl. Acad. Sci. U.S.A.* **116**, 17701 (2019).
53. J. Custers *et al*., Destruction of the Kondo effect in the cubic heavy-fermion compound $Ce_3Pd_{20}Si_6$. *Nat. Mater.* **11**, 189 (2012).
54. R. Shiina, H. Shiba, P. Thalmeier, Magnetic-field effects on quadrupolar ordering in a Γ_8-quartet system CeB_6. *J. Phys. Soc. Jpn.* **66**, 1741 (1997).
55. K.-A. Lorenzer, "Quantum critical behaviour in cubic heavy-fermion compounds," PhD thesis, Vienna University of Technology (2012).
56. H. Hu, L. Chen, Q. Si, Extended dynamical mean field theory for correlated electron models. arXiv [Preprint] (2022). http://arxiv.org/abs/2210.14197 (Accessed 6 July 2023).
57. Q. Si, J. L. Smith, Kosterlitz-Thouless transition and short range spatial correlations in an extended Hubbard model. *Phys. Rev. Lett.* **77**, 3391 (1996).
58. J. Smith, Q. Si, Spatial correlations in dynamical mean-field theory. *Phys. Rev. B* **61**, 5184 (2000).
59. R. Chitra, G. Kotliar, Effective-action approach to strongly correlated fermion systems. *Phys. Rev. B* **63**, 115110 (2001).
60. L. Zhu, Q. Si, Critical local-moment fluctuations in the Bose-fermi Kondo model. *Phys. Rev. Lett.* **66**, 024426 (2002).
61. Q. Si, J. Smith, Kosterlitz-Thouless transition and short range spatial correlations in an extended Hubbard model. *Phys. Rev. Lett.* **77**, 3391 (1996).
62. J. Smith, Q. Si, Non-Fermi liquids in the two-band extended Hubbard model. *Europhys. Lett.* **45**, 228 (1999).
63. J. Smith, "Non-Fermi liquid states in strongly correlated electron systems," PhD thesis (2000).
64. Here we ignore a unstable fixed point $(y_1^*, y^*, M^*) = \left(\frac{\sqrt{\epsilon}}{2}, 0, \frac{1}{2}\right)$; because the RG trajactories around it can flow toward the generic critical point $\left(0, \frac{\sqrt{\epsilon}}{2}, 1\right)$, it does not influence the structure of the RG flow diagram (Fig. 3).
65. S. Chakravarty, J. E. Hirsch, Approximate mapping of the two-impurity symmetric Anderson model in the local-moment regime to a classical problem. *Phys. Rev. B* **25**, 3273 (1982).
66. A. O. Caldeira, A. J. Leggett, Quantum tunnelling in a dissipative system. *Ann. Phys. (N.Y.)* **149**, 374 (1983).
67. J. Cardy, One-dimensional models with $1/r^2$ interactions. *J. Phys. A: Math. Gen.* **14**, 1407 (1981).
68. Q. Si, G. Kotliar, Metallic non-Fermi-liquid phases of an extended Hubbard model in infinite dimensions. *Phys. Rev. B* **48**, 13881 (1993).